


Cite this: *RSC Adv.*, 2021, **11**, 27453

## Efficient and reusable ordered mesoporous $\text{WO}_x/\text{SnO}_2$ catalyst for oxidative desulfurization of dibenzothiophene<sup>†</sup>

Wenxiang Piao,<sup>‡a</sup> Zhenghua Li,<sup>‡b</sup> Chengbin Li,<sup>b</sup> Jin Seo Park,<sup>b</sup> Jung-ho Lee,<sup>b</sup> Zhengyang Li,<sup>b</sup> Ki Yeong Kim,<sup>b</sup> Long Yi Jin,<sup>ID \*a</sup> Ji Man Kim,<sup>ID \*b</sup> and Mingshi Jin,<sup>ID \*a</sup>

The oxidative desulfurization (ODS) of organic sulfur compounds over tungsten oxide supported on highly ordered mesoporous  $\text{SnO}_2$  ( $\text{WO}_x/\text{meso-SnO}_2$ ) was investigated. A series of  $\text{WO}_x/\text{meso-SnO}_2$  with  $\text{WO}_x$  contents from 10 wt% to 30 wt%, were prepared by conventional wet impregnation. The physico-chemical properties of the  $\text{WO}_x/\text{meso-SnO}_2$  catalysts were characterized by X-ray diffraction (XRD),  $\text{N}_2$  adsorption–desorption isotherms, electron microscopy, Fourier transform infrared spectroscopy (FT-IR), Raman spectroscopy, and the temperature-programmed reduction of hydrogen ( $\text{H}_2\text{-TPR}$ ). The characterization results indicated that these catalysts possessed mesoporous structures with uniform pores, high specific surface areas, and well-dispersed polyoxotungstate species on the surface of meso- $\text{SnO}_2$  support. The ODS performances were evaluated in a biphasic system (model oil/acetonitrile,  $S_{\text{initial}} = 2000$  ppm), using  $\text{H}_2\text{O}_2$  as an oxidant, and acetonitrile as an extractant. Dibenzothiophene (DBT) in the model oil was removed completely within 60 min at 50 °C using 20 wt%  $\text{WO}_x/\text{meso-SnO}_2$  catalyst. Additionally, the effect of reaction temperature,  $\text{H}_2\text{O}_2/\text{DBT}$  molar ratio, amount of catalyst and different sulfur-containing substrates on the catalytic performances were also investigated in detail. More importantly, the 20 wt%  $\text{WO}_x/\text{meso-SnO}_2$  catalyst exhibited 100% sulfur-removal efficiency without any regeneration process, even after six times recycling.

Received 26th June 2021  
Accepted 30th July 2021

DOI: 10.1039/d1ra04957g  
rsc.li/rsc-advances

## 1. Introduction

Sulfur-containing compounds in transportation fuels are converted to  $\text{SO}_x$ , which is a major source of air pollution and energy corrosion.<sup>1</sup> Thus, removal of sulfur has become an important research subject worldwide, and many countries have legislated environmental regulations that limit sulfur content in fuels to be below 10 ppm.<sup>2</sup> To date, hydrodesulfurization (HDS) is a conventional desulfurization method in the petroleum refining industry for the removal of sulfur in fuels, including thiols, thioethers, and disulfides. However, the HDS process has some respective disadvantages. For example, HDS requires severe operation conditions at high pressure of (20–100) atm of  $\text{H}_2$  and temperatures (300–400 °C).<sup>3</sup> Additionally, it is difficult to remove refractory sulfides, such as benzothiophene (BT), dibenzothiophene (DBT), and their derivatives, owing to their steric hindrance, and low electron density around

sulfur atom.<sup>4</sup> Therefore, alternative processes have been suggested to overcome these drawbacks. So far, several alternative deep desulfurization technologies, such as adsorption,<sup>5,6</sup> extraction,<sup>7,8</sup> bioprocess,<sup>9,10</sup> oxidation,<sup>11–13</sup> and photocatalytic oxidation desulfurization<sup>14,15</sup> have been extensively investigated.

Among these processes, oxidative desulfurization (ODS) combined with extraction process is considered to be one of the most promising processes. It can be operated at atmospheric pressure and low temperature without consuming hydrogen. During this process, organic sulfides can be oxidized into highly polar sulfones and sulfoxides by catalysts with suitable oxidants, and removed by the subsequent extraction process using polar organic solvents. Various oxidants have been used for the oxidation of sulfur compounds, including molecular oxygen,<sup>16–18</sup> ozone,<sup>19</sup> organic peroxide,<sup>20</sup> and hydrogen peroxide ( $\text{H}_2\text{O}_2$ ).<sup>21,22</sup> Among them,  $\text{H}_2\text{O}_2$  has been extensively used, due to its high activity, high oxidative capacity, and production of only water after the reaction.

In the field of heterogeneous catalysis, it is well-known that group 5 and 6 metals (e.g., Mo, W, V) in high oxidation states can react with hydrogen oxide to produce peroxometallate complexes, which are efficient catalysts for oxidative desulfurization reaction.<sup>8,23,24</sup> Caero *et al.* examined the ODS of a real diesel fuel on  $\text{V}_2\text{O}_5$  supported on alumina, silica, niobia, ceria, and titania, and reported that an approximately 99% decrease

<sup>a</sup>Department of Chemistry, Park Road 977, Yanji City, Jilin Province 133002, P. R. China. E-mail: lyjin@ybu.edu.cn; jimankim@skku.edu; msjin1231@ybu.edu.cn

<sup>b</sup>Department of Chemistry, Sungkyunkwan University, Suwon, 440-746, Republic of Korea

† Electronic supplementary information (ESI) available. See DOI: 10.1039/d1ra04957g

‡ These authors contributed equally.



in the initial amount of sulfur.<sup>25</sup> Prasad *et al.* reported that  $\text{MoO}_3/\text{Al}_2\text{O}_3-\text{SiO}_2$  catalyst had the best catalytic performance for ODS of 4,6-dimethylbenzothiophene (4,6-DMDBT) with *tert*-butyl hydroperoxide.<sup>26</sup> A novel composite catalyst  $\text{V}_\text{o}-\text{MoO}_2/\text{NC}$  exhibited excellent ODS activity and reusability, which was ascribed essentially to the strong electron-donating effect of NC on  $\text{V}_\text{o}-\text{MoO}_2$ .<sup>27</sup> Additionally, tungsten-based catalysts have also been extensively studied for ODS reaction in both single and biphasic liquid phase operating systems, due to the tungsten-oxo species on the surface of catalysts as active sites being combined with  $\text{H}_2\text{O}_2$  to form peroxy-tungsten intermediates ( $\text{W}-\text{O}-\text{O}-\text{H}$ ), contributing to the conversion of DBT to DBTO<sub>2</sub> in the oxidation process.<sup>28</sup> In order to improve the activity and stability of catalysts, tungsten species are dispersed on various supports such as  $\text{W}-\text{MCM}-41$ ,<sup>29</sup>  $\text{WO}_3-\text{SBA}-15$ ,<sup>30</sup>  $\text{WO}_x/\text{TiO}_2$ ,<sup>31</sup>  $\text{WO}_x-\text{ZrO}_2$ ,<sup>32</sup>  $\text{WO}_3/\text{MoO}_3/\text{Al}_2\text{O}_3$ ,<sup>33</sup> and  $\text{Mo}/\text{KIT}-6-\text{Ti}$ .<sup>34</sup>

Recently,  $\text{SnO}_2$ -based heterogeneous catalyst containing tungsten oxide has been reported, exhibiting efficient selective oxidation of amines and sulfides with green oxidant  $\text{H}_2\text{O}_2$ , has been reported.<sup>35</sup> Zhang *et al.* have prepared  $\text{WO}_3/\text{SnO}_2$  composite catalysts by the co-precipitation impregnation method for selective the oxidation of 1,2-benzenedimethanol to phthalide using  $\text{H}_2\text{O}_2$  as oxidant, suggesting that high dispersion of tungsten species on  $\text{SnO}_2$  can improve catalytic activity in reaction.<sup>36</sup> Ma *et al.* have found that the  $\text{SnO}_2-\text{WO}_3$  composite as solid acid catalyst is more effective than pure  $\text{WO}_3$  and  $\text{SnO}_2$  catalysts in the hydrolysis of dichlorodifluoromethane, due to the strong interaction between  $\text{WO}_3$  and  $\text{SnO}_2$ .<sup>37</sup> According to the above reports,  $\text{SnO}_2$  will be a good choice as support to disperse  $\text{WO}_3$  for ODS reaction.

In the present work, highly ordered mesoporous  $\text{SnO}_2$  (meso- $\text{SnO}_2$ ) was successfully prepared from KIT-6 silica template using a nano-replication method.  $\text{WO}_x$  species were then highly dispersed on the meso- $\text{SnO}_2$  support by an incipient wet-impregnation method. The Deep desulfurization performance of  $\text{WO}_x/\text{meso-}\text{SnO}_2$  catalysts for fuel oil in a biphasic (model oil/acetonitrile) system under different reaction conditions was investigated in detail. The  $\text{WO}_x/\text{meso-}\text{SnO}_2$  catalyst with 20 wt%  $\text{WO}_x$  loading showed excellent catalytic performance in removing DBT, BT, and 4,6-DMDBT, because when  $\text{WO}_x$  species interacted with  $\text{SnO}_2$ , a lot of active species (tungsten oxo-species,  $\text{W}=\text{O}$ ) were generated. Furthermore, the catalysts with high surface area, large pore size, and 3D pore network are beneficial for the diffusion and transport of reactants and products during ODS reaction. In addition, the reusability and stability of the catalyst were investigated.

## 2. Experimental

### 2.1 Synthesis of KIT-6 silica template

The typical synthesis of the mesoporous KIT-6 silica template was similar to the process described in the literature.<sup>38,39</sup> A triblock copolymer (pluronic P123,  $\text{EO}_{20}\text{PO}_{70}\text{EO}_{20}$ , Aldrich) was dissolved in distilled water and *n*-butanol solvent was added to the mixture at room temperature. The solution was vigorously stirred for 6 h to obtain a clear polymer solution. The clear solution was then kept in a water bath at 35 °C for 24 h followed by the addition of

hydrochloric acid (HCl, Samchun) and tetraethylorthosilicate (TEOS, Samchun) with magnetic stirring. The molar composition of the mixture was P123 : BuOH : TEOS : HCl :  $\text{H}_2\text{O} = (0.017 : 1.01 : 1.33 : 0.45 : 198)$ . After that, the mixture was kept in an oven at 100 °C for another 24 h. The white precipitates were filtered and washed with distilled water and ethanol to completely remove the block copolymer. Finally, the product was calcined at 550 °C for 3 h in air.

### 2.2 Synthesis of ordered mesoporous $\text{SnO}_2$

Ordered mesoporous  $\text{SnO}_2$  (meso- $\text{SnO}_2$ ) material was prepared by a nano-replication method using mesoporous KIT-6 as silica template. The meso- $\text{SnO}_2$  material was synthesized by a solvent-free infiltration method.<sup>40</sup> Typically, 5.09 g  $\text{SnCl}_2 \cdot 2\text{H}_2\text{O}$  (Aldrich) was melted at 100 °C to liquid states. It was then impregnated into 5.0 g of preheated silica template. The composite materials were shaken for 1 h, and put in an oven at 80 °C overnight, in order to let the precursor spontaneously infiltrate into mesopores of the silica template. The composite material was then calcined at 700 °C for 3 h under static air condition. After that, the silica template was removed from the composite by a wet-etching process using a 20 wt% hydrofluoric acid (HF) solution. The resulting solid product was washed with distilled water and acetone several times, and then dried at 80 °C overnight in an oven.

### 2.3 Synthesis of $\text{WO}_x/\text{meso-}\text{SnO}_2$ catalysts

$\text{WO}_x$ -Supported catalysts were prepared by an incipient wetness impregnation method. To obtain 20 wt%  $\text{WO}_x/\text{meso-}\text{SnO}_2$ , an aqueous solution of  $(\text{NH}_4)_6\text{W}_{12}\text{O}_{40} \cdot x\text{H}_2\text{O}$  (0.266 g, Aldrich) was impregnated into 1.0 g of meso- $\text{SnO}_2$ . After drying at 80 °C overnight, the obtained product was heated at 400 °C for 3 h under static air condition.  $\text{WO}_x/\text{meso-}\text{SnO}_2$  with (10 and 30) wt% loadings were also prepared through the same method.

### 2.4 Characterization

The X-ray diffraction (XRD) patterns of these prepared catalysts were obtained from a Rigaku D/MAX-2200 ultima equipped with  $\text{Cu K}\alpha$  radiation ( $\lambda = 1.54 \text{ \AA}$ ) at 30 kV and 40 mA.  $\text{N}_2$  adsorption-desorption isotherms were obtained using a Micromeritics Tristar system at liquid  $\text{N}_2$  temperature. Before measurements, samples were degassed at 323 K for 12 h. The Brunauer-Emmett-Teller (BET) and Barrett-Joyner-Halenda (BJH) methods were utilized to calculate the BET surface area and pore size distribution, respectively. Scanning electron microscopy (SEM) image was obtained using a Hitachi UHR S 5500 FE-SEM operated at an accelerating voltage of 15 kV. Transmission electron microscopy (TEM) images were collected using JEOL JEM 3010 at an accelerating voltage of 200 kV. Raman spectra were recorded under ambient conditions at room temperature (RT) using WITEC Alpha300. The excitation line of the laser was at 532 nm. Fourier transform infrared spectroscopy (FT-IR) spectra were measured using KBr wafer technique with Bruker IFS-66 spectrometer.  $\text{H}_2$ -Temperature programmed reduction ( $\text{H}_2\text{-TPR}$ ) was performed in a fixed-bed reactor. Sample (20 mg) was put in a quartz microreactor, and pretreated with He up to



100 °C at a rate of 10 °C min<sup>-1</sup> for 1 h for pretreatment. Then 10 vol% H<sub>2</sub> in a He flow of 40 mL min<sup>-1</sup> was maintained at RT for 30 min. Finally, the sample was ramped to 900 °C at 10 °C min<sup>-1</sup>.

## 2.5 Catalytic performance

Sulfur-containing compound (DBT, BT, or 4,6-DMDBT) was dissolved in *n*-heptane using a corresponding S-content of 2000 ppm as model oil. A typical ODS reaction of model oil was carried out in a 100 mL two-necked flask by adding 0.1 g catalyst, 0.27 mL of 34.5% H<sub>2</sub>O<sub>2</sub> aqueous solution, 14 mL of acetonitrile, and 14 mL of the model oil successively into the flask, followed by vigorously mixing with a magnetic stirrer at 50 °C for 2 h under atmospheric pressure. Reaction products (upper oil layer) were analyzed by gas chromatography–flame ionization detector (GC-FID) equipped with a HP-5 capillary column (30 m × 0.32 mm inner diameter × 1.0 μm film thickness).

## 3. Results and discussion

### 3.1 Catalyst characterization

Fig. 1 shows the low- and high-angle XRD patterns for the KIT-6 template (inset), meso-SnO<sub>2</sub>, and WO<sub>x</sub>/meso-SnO<sub>2</sub> materials. In the low-angle XRD patterns (Fig. 1A), KIT-6 exhibited typical diffraction peaks (211), (220), and (332), which are characteristic of the cubic *Ia3d* mesostructure. The meso-SnO<sub>2</sub> and WO<sub>x</sub>/meso-SnO<sub>2</sub> materials exhibited two narrow and well-defined peaks (110) and (211), indicating the highly ordered mesostructure of all materials. The presence of new diffraction peak (110) around 0.60° indicated that after the silica template etching process the cubic *Ia3d* mesostructure of KIT-6 silica template transformed into tetragonal *I4<sub>1</sub>/a* (or lower symmetry).<sup>41</sup> In the wide-angle XRD patterns (Fig. 1B), diffraction peaks of meso-SnO<sub>2</sub> with 2θ/degree values corresponding to (110), (101), (200), (211), (220), (002), (310), (301), (202), and (321) planes exhibited a typical tetragonal phase of SnO<sub>2</sub> (JCPDS 21-1250, *P4<sub>2</sub>/mm*). After loading (10 and 20) wt% WO<sub>x</sub> on meso-SnO<sub>2</sub>, there was no diffraction line of the tungsten oxide species in wide angle patterns, revealing that the WO<sub>x</sub> existed mainly in amorphous phases or particles size was very small, and they were finely dispersed on the meso-SnO<sub>2</sub> support. The diffraction peaks of crystalline WO<sub>3</sub> appeared when 30 wt% WO<sub>x</sub> was loaded on meso-SnO<sub>2</sub>, as shown in Fig. 1B. Table 1 summarizes the crystallite sizes of all materials that were calculated using the Debye–Scherrer equation.

Mesostructures of KIT-6, meso-SnO<sub>2</sub>, and WO<sub>x</sub>/meso-SnO<sub>2</sub> materials were confirmed by N<sub>2</sub> adsorption–desorption measurements (Fig. S1†). As shown in Fig. S1(a) and (c),† all the materials exhibited typical type-IV isotherms with H1 hysteresis loop in the range of  $p/p_0 = 0.5$ –1.0, as characteristics of mesoporous materials. The corresponding pore size distribution curve calculated from the adsorption of N<sub>2</sub>-sorption isotherm showed that KIT-6 only had one porous structure (Fig. S1(b)†), whereas the meso-SnO<sub>2</sub> and WO<sub>x</sub>/meso-SnO<sub>2</sub> materials exhibited dual porous structures (Fig. S1(d)†). The smaller pore sizes

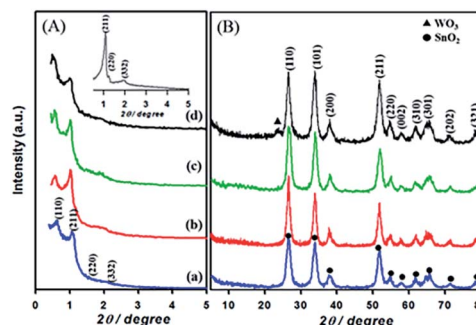


Fig. 1 (A) Low- and (B) high-angle patterns of samples. (a) Meso-SnO<sub>2</sub>, (b) 10 wt% WO<sub>x</sub>/meso-SnO<sub>2</sub>, (c) 20 wt% WO<sub>x</sub>/meso-SnO<sub>2</sub>, (d) 30 wt% WO<sub>x</sub>/meso-SnO<sub>2</sub>, and KIT-6 (inset A).

of (2.5–3.3) nm come from the silica wall of the KIT-6 template, while the larger pore sizes (above 10 nm) are caused by the phase-transformation from the cubic *Ia3d* mesostructure to the tetragonal *I4<sub>1</sub>/a* (or lower) mesostructure. The surface area, total pore volume, and pore size for KIT-6 were 725 m<sup>2</sup> g<sup>-1</sup>, 0.83 cm<sup>3</sup> g<sup>-1</sup>, and 7.0 nm, respectively. Table 1 summarizes the physical properties of meso-SnO<sub>2</sub> and WO<sub>x</sub>/meso-SnO<sub>2</sub> materials and shows that after loading different amounts of WO<sub>x</sub> on meso-SnO<sub>2</sub> support, the surface areas, pore volumes, and pore sizes of samples were decreased, probably due to the partial pore blockage by the impregnated WO<sub>x</sub>. Compared to the recalcinated meso-SnO<sub>2</sub>, pure meso-SnO<sub>2</sub> combined with WO<sub>x</sub> could suppress the particle agglomeration during the sintering process, due to the cooperative nature of the cations of the mixed oxides.<sup>42</sup>

The SEM (Fig. 2a–d) and TEM images (Fig. 2e–h) also confirm the meso-SnO<sub>2</sub> and WO<sub>x</sub>/meso-SnO<sub>2</sub> materials with regular porosity and well-defined crystalline frameworks. All the materials consisted of well-defined nanopores and frameworks with uniformly repeating units over the whole particle, indicating that the highly ordered mesostructure remained before and after loading works. The W/Sn ratios of the WO<sub>x</sub>/meso-SnO<sub>2</sub> materials with different amounts of WO<sub>x</sub> loading were obtained by Energy dispersed X-ray spectroscopy (EDX) from SEM analysis (Table 1), indicating that the tungsten content increased with increasing the amount of WO<sub>x</sub> loading. High-resolution TEM images (inset of TEM images) indicated that the meso-SnO<sub>2</sub> and (10 and 20) wt% WO<sub>x</sub>/meso-SnO<sub>2</sub> materials exhibited well-formed crystalline framework structures. The *d*-spacings of 3.41, 2.68 and 2.35 Å correspond to the (110), (101) and (200) planes of the tetragonal phase of SnO<sub>2</sub>, indicating that the WO<sub>x</sub> was finely dispersed on the surface of meso-SnO<sub>2</sub>, without aggregation. Fig. 2h shows that the catalyst with 30 wt% WO<sub>x</sub> loading mainly displayed the crystal SnO<sub>2</sub> structure with tiny WO<sub>3</sub> structure with *d*-spacing of 3.85 Å, which was indexed to the (001) plane of the orthorhombic WO<sub>3</sub> phase.<sup>43</sup> EDX mapping images obtained from TEM analysis revealed that the tungsten atoms in WO<sub>x</sub>/meso-SnO<sub>2</sub> materials were homogeneously dispersed over the whole particles as shown in Fig. 2j–l.

Fig. 3 shows the Raman spectra of meso-SnO<sub>2</sub> and WO<sub>x</sub>/meso-SnO<sub>2</sub> materials in the spectral range of 200 to 1200 cm<sup>-1</sup>.



Table 1 Physical properties of meso-SnO<sub>2</sub> and X wt% WO<sub>x</sub>/meso-SnO<sub>2</sub>

Materials	$S_{\text{BET}}^a$ (m <sup>2</sup> g <sup>-1</sup> )	$V_{\text{tot}}^b$ (cm <sup>3</sup> g <sup>-1</sup> )	$D_p^c$ (nm)	$D^d$ (nm)	W/Sn <sup>e</sup>
Meso-SnO <sub>2</sub>	132	0.41	2.8/20.3	6.9	—
10 wt% WO <sub>x</sub> /meso-SnO <sub>2</sub>	90	0.18	2.8/17.0	8.3	9.10
20 wt% WO <sub>x</sub> /meso-SnO <sub>2</sub>	78	0.11	2.9/16.4	7.2	19.60
30 wt% WO <sub>x</sub> /meso-SnO <sub>2</sub>	57	0.07	2.8/16.5	7.6	27.86
(R) meso-SnO <sub>2</sub> <sup>f</sup>	73	0.31	3.3/18.0	9.2	—

<sup>a</sup> Surface areas were calculated by the BET method from N<sub>2</sub> adsorption isotherms in the range of  $p/p_0 = 0.05$ –0.20. <sup>b</sup> Total pore volumes were calculated from the N<sub>2</sub> adsorption data at  $p/p_0 = 0.99$ . <sup>c</sup> Pore sizes were obtained from the adsorption branches of N<sub>2</sub> sorption isotherms by the BJH method. <sup>d</sup> Crystallite sizes were calculated using Scherrer's equation from the high-angle XRD patterns. <sup>e</sup> Surface Sn/W calculated from the SEM-EDX results. <sup>f</sup> R represents the meso-SnO<sub>2</sub> was re-calcined at 400 °C for 3 h such as WO<sub>x</sub>/meso-SnO<sub>2</sub> catalyst.

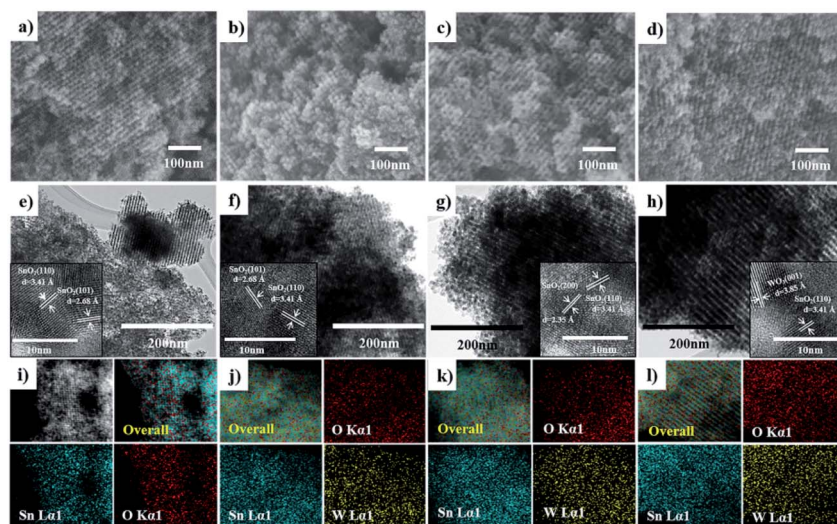


Fig. 2 Electron images of all the prepared materials. (a–d) Representative SEM images, (e–h) representative TEM images with high-resolution TEM images (inset), and (i–l) elemental mapping images of meso-SnO<sub>2</sub>, 10 wt% WO<sub>x</sub>/meso-SnO<sub>2</sub>, 20 wt% WO<sub>x</sub>/meso-SnO<sub>2</sub>, and 30 wt% WO<sub>x</sub>/meso-SnO<sub>2</sub>.

The spectrum of meso-SnO<sub>2</sub> showed the bands at around 476 cm<sup>-1</sup> (E<sub>g</sub>), 633 cm<sup>-1</sup> (A<sub>1g</sub>), and 774 cm<sup>-1</sup> (B<sub>2g</sub>) that could be assigned to the tetragonal structure of SnO<sub>2</sub>.<sup>44</sup> After loading tungsten species, the prominent A<sub>1g</sub> band was shifted to higher wave numbers than that of pure meso-SnO<sub>2</sub>, indicating the presence of interaction between WO<sub>x</sub> species and SnO<sub>2</sub>.<sup>45</sup> Simultaneously, the broad band appeared in the 200–400 cm<sup>-1</sup> region was attributed to the W–O–W bending modes.<sup>46</sup> The new band at around 960–980 cm<sup>-1</sup> appeared in all the WO<sub>x</sub>/meso-SnO<sub>2</sub> materials was attributed to the terminal W=O bonds of surface WO<sub>x</sub> species. The shift of surface W=O band from 960 cm<sup>-1</sup> to 980 cm<sup>-1</sup> with increasing the WO<sub>x</sub> loading might be related to the polymerization of surface monooxo tungsten species.<sup>47</sup> With further increase in WO<sub>x</sub> loading (30 wt%), three new bands at about 272 cm<sup>-1</sup>, 715 cm<sup>-1</sup> and 807 cm<sup>-1</sup> were observed. This can be assigned to asymmetric and symmetric stretching vibration of W–O–W modes and W=O stretching modes. It is noteworthy that the formation of crystalline WO<sub>3</sub> phase as observed in XRD and TEM measurements.<sup>48</sup>

The FT-IR spectra of meso-SnO<sub>2</sub> and the WO<sub>x</sub>/meso-SnO<sub>2</sub> materials with different WO<sub>x</sub> contents are presented in Fig. S2.†

As reported in the literature,<sup>49</sup> the peaks at 651 cm<sup>-1</sup> and 553 cm<sup>-1</sup> could be assigned to different vibration modes of O–Sn–O and Sn–O–Sn groups. For WO<sub>x</sub>/meso-SnO<sub>2</sub> materials,

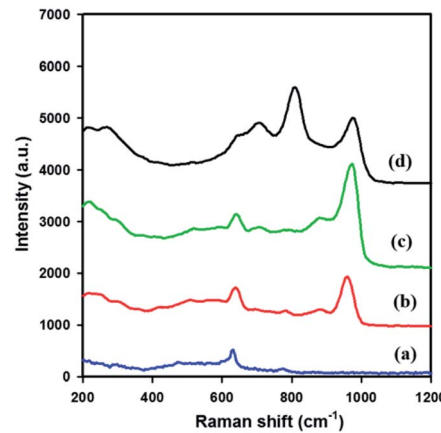


Fig. 3 Raman spectra of (a) meso-SnO<sub>2</sub>, (b) 10 wt% WO<sub>x</sub>/meso-SnO<sub>2</sub>, (c) 20 wt% WO<sub>x</sub>/meso-SnO<sub>2</sub>, and (d) 30 wt% WO<sub>x</sub>/meso-SnO<sub>2</sub>.



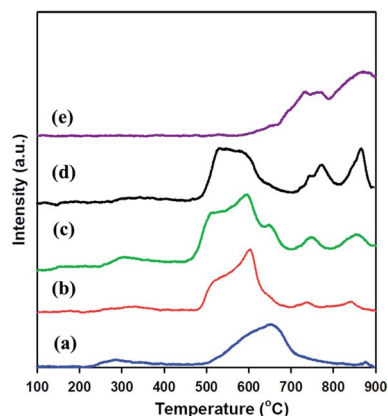


Fig. 4  $\text{H}_2$ -TPR Profiles of (a) meso- $\text{SnO}_2$ , (b) 10 wt%  $\text{WO}_x$ /meso- $\text{SnO}_2$ , (c) 20 wt%  $\text{WO}_x$ /meso- $\text{SnO}_2$ , and (d) 30 wt%  $\text{WO}_x$ /meso- $\text{SnO}_2$ .

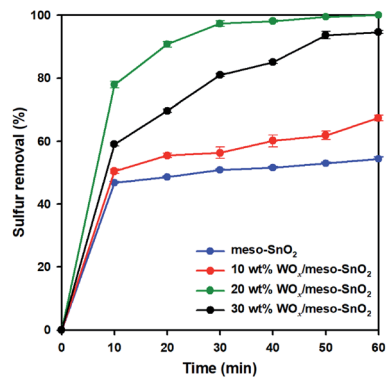


Fig. 5 Effect of different catalyst on removal of DBT from mode oil. Reaction conditions: mode oil = 14 mL, acetonitrile = 14 mL, sulfur concentration = 2000 ppm, catalyst = 0.1 g,  $n[\text{H}_2\text{O}_2] : n[\text{S}] = 5 : 1$ , reaction temperature = 50 °C, time = 60 min.

a peak appeared at  $970\text{ cm}^{-1}$  was assigned to the stretching modes of W–O bond or W=O bond. Another new peak at  $868\text{ cm}^{-1}$  demonstrated the typical Sn–O–W modes,<sup>50</sup> indicating the presence of strong interactions between highly dispersed  $\text{WO}_x$  and meso- $\text{SnO}_2$ . Additionally, the peak at  $1621\text{ cm}^{-1}$  was attributed to the bending vibrations of

hydrogen-bonded surface OH groups of physically adsorbed water molecules.<sup>51</sup>

$\text{H}_2$ -TPR was examined to investigate the reducibility of meso- $\text{SnO}_2$  and  $\text{WO}_x$ /meso- $\text{SnO}_2$  catalysts. As shown in Fig. 4, the TPR profile of bulk  $\text{WO}_3$  exhibited two high intensity peaks of hydrogen consumed beginning at 600 °C, centered at 770 and 870 °C. It is important to note that these peaks might be assigned to the stepwise reduction of  $\text{WO}_3$  to W [ $\text{WO}_3 \rightarrow \text{W}_{20}\text{O}_{58} \rightarrow \text{WO}_2 \rightarrow \text{W}$ ].<sup>52</sup> The TPR profile of pure meso- $\text{SnO}_2$  exhibited a mainly reduction peak at about 652 °C, which could be assigned to the reduction of  $\text{Sn}(4+) \rightarrow \text{Sn}(2+) \rightarrow \text{Sn}(0)$ . After impregnated  $\text{WO}_x$ , the first reduction peaks of all the  $\text{WO}_x$ /meso- $\text{SnO}_2$  catalysts shifted to lower temperature, indicating the presence of interaction between  $\text{WO}_x$  species and meso- $\text{SnO}_2$  support. Simultaneously, the relative area of this reduction peak increased with increasing  $\text{WO}_x$  concentration due to the increasing fraction of  $\text{WO}_x$  species in domains. The reduction temperature of the first peak at 450–550 °C was probably attributed to the reduction of octahedrally coordinated  $\text{WO}_x$  species as reported by Wachs *et al.*<sup>53</sup> Octahedrally coordinated  $\text{WO}_x$  species were found to be reduced at temperatures varying from 300 to 600 °C through intermediate oxidation states. Accordingly, the reduction peaks at 450–700 °C were assigned to the  $\text{WO}_3$  to  $\text{WO}_{2.9}$  (or  $\text{WO}_2$ ) reduction process and the reduction of  $\text{SnO}_2$ . The other two peaks located at higher temperature between 740 °C and 900 °C were probably attributed to a further reduction process of partially reduced  $\text{WO}_x$  species ( $\text{WO}_{2.9} \rightarrow \text{WO}_2 \rightarrow \text{W}$ ) formed in the first reduction peak, together with the reduction of tetrahedrally coordinated  $\text{WO}_x$  species that interacted with  $\text{SnO}_2$  support.<sup>54,55</sup> In the case of 30 wt%  $\text{WO}_x$ /meso- $\text{SnO}_2$  catalyst, there were three reduction peaks centered at 743, 770, 867 °C, similar to those of bulk  $\text{WO}_3$ , indicating the formation of crystalline  $\text{WO}_3$  on the surface of meso- $\text{SnO}_2$  support. In the case of 30 wt%  $\text{WO}_x$ /meso- $\text{SnO}_2$  catalyst, there were three reduction peaks centered at 743, 770 and 867 °C, similar to those of bulk  $\text{WO}_3$ , indicating the formation of crystalline  $\text{WO}_3$  on the surface of meso- $\text{SnO}_2$  support.

### 3.2 Catalytic study

Fig. 5 shows the catalytic performance of pure meso- $\text{SnO}_2$  and  $\text{WO}_x$ /meso- $\text{SnO}_2$  catalysts for the removal of DBT from model oil, which were carried out at 50 °C with  $\text{H}_2\text{O}_2$  as oxidant for 2 h.

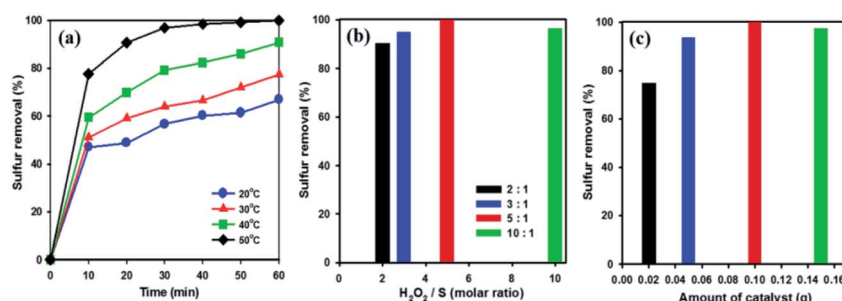


Fig. 6 Effect of (a) reaction temperatures, (b) molar ratio of  $\text{H}_2\text{O}_2/\text{S}$ , and (c) amount of catalyst on removal of DBT from model oil over 20 wt%  $\text{WO}_x$ /meso- $\text{SnO}_2$  catalyst reaction conditions: model oil = 14 mL, sulphur concentration = 2000 ppm, catalyst = 0.1 g,  $n[\text{H}_2\text{O}_2] : n[\text{S}] = 5 : 1$ , time = 60 min.

$\text{WO}_x$  supported catalysts ( $\text{WO}_x/\text{meso-SnO}_2$ ) exhibited better catalytic performance than pure  $\text{SnO}_2$  support because the surface tungsten-oxo species ( $\text{W}=\text{O}$ ) as the active sites could interact with  $\text{H}_2\text{O}_2$  to form surface peroxy-tungsten ( $\text{W}-\text{O}-\text{O}-\text{H}$ ) species, and then DBT was oxidized to  $\text{DBTO}_2$  *via* oxidation process.<sup>56</sup> Therefore, the amount of  $\text{WO}_x$  loaded on meso- $\text{SnO}_2$  immensely influenced the desulfurization efficiency. As shown in Fig. 5, the desulfurization efficiency of  $\text{WO}_x$ -supported catalysts was remarkably increased with increasing  $\text{WO}_x$  concentration and reached the 100% removal with 20 wt%  $\text{WO}_x$  loading. The reason is because the active sites of tungsten-oxo species of 20 wt%  $\text{WO}_x/\text{meso-SnO}_2$  catalyst are more than those of other catalysts. Further increase the  $\text{WO}_x$  loading up to 30 wt% resulted in the decrease catalytic removal of DBT (94.5%). This phenomenon may be ascribed to the excess of 20 wt%  $\text{WO}_x$  caused aggregation of tungsten oxide on the surface of meso- $\text{SnO}_2$  and the formation of crystalline  $\text{WO}_3$  lead to a smaller surface area as shown in BET results (Table 1).

In order to examine the influence of reaction temperatures on the removal of DBT, a series of experiments were performed at different temperatures using 20 wt%  $\text{WO}_x/\text{meso-SnO}_2$  catalyst. As shown in Fig. 6(a), raising the reaction temperature from 20 °C to 50 °C resulted in a remarkable increase in DBT removal efficiency and complete removal at 50 °C after 60 min. This indicates that the higher temperature is beneficial for  $\text{H}_2\text{O}_2$  oxidation because the higher oxidation reaction rate at low temperatures might be limited by kinetics.<sup>57</sup> According to the above analysis, 50 °C was chosen as the optimal reaction temperature in this work.

$\text{H}_2\text{O}_2$  is one of the main factors in oxidative system. Hence, oxidative desulfurization of DBT was carried out under different molar ratios (from 2 to 10) of  $\text{H}_2\text{O}_2/\text{S}$  at 50 °C with 20 wt%  $\text{WO}_x/\text{meso-SnO}_2$  as catalyst. As shown in Fig. 6(b), the DBT removal efficiency was increased with increasing the molar ratio of  $\text{H}_2\text{O}_2/\text{S}$  from 2 to 5 followed by a slight decreased at molar ratio of 10. This indicates that the excess oxidant is beneficial for increasing the reaction efficiency in heterogeneous catalysis.<sup>58</sup> According to the stoichiometry of the ODS reaction, 2 mole of  $\text{H}_2\text{O}_2$  are consumed for the conversion of 1 mole of sulfur-containing compounds to their corresponding sulfones ( $\text{DBTO}_2$ ).<sup>59</sup> However, the molar ratio of 2 gives only 90.3% of the sulfur removal, whereas the DBT can be removed completely from the model oil at the  $\text{H}_2\text{O}_2/\text{S}$  molar ratio of 5. The optimum ratio of  $\text{H}_2\text{O}_2/\text{S}$  was found to be 5, indicating that the  $\text{H}_2\text{O}_2$  not only reacting with DBT, but also taken its self-decomposition. Therefore, stoichiometric amount of  $\text{H}_2\text{O}_2$  can not result in complete oxidation of DBT under the present reaction conditions.

The amount of catalyst also affects desulfurization efficiency on the removal of DBT. As shown in Fig. 6(c), the sulfur removal increased from 74.7% to 100% in 60 min, when the amount of catalyst increased from 0.02 to 0.1 g. Below 0.1 g catalyst amount, the active sites of the catalyst were not enough to catalysis oxidative oxidize DBT completely. Nevertheless, when the catalyst amount increased to 0.15 g, the removal efficiency for DBT decreased to 97.2%. Therefore, the excessive catalyst was unnecessary in the desulfurization reaction because the excess active sites of catalyst might be covered by the absorption and

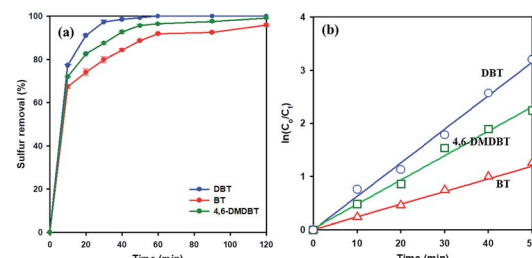


Fig. 7 (a) Oxidative desulfurization of different sulfur-containing compounds over 20 wt%  $\text{WO}_x/\text{meso-SnO}_2$  catalyst. (b) Pseudo-first-order kinetics for DBT, BT, 4,6-DMDBT. Reaction conditions: model oil = 14 mL, acetonitrile = 14 mL, sulfur concentration = 2000 ppm, catalyst = 0.1 g,  $n[\text{H}_2\text{O}_2] : n[\text{S}] = 5 : 1$ , time = 120 min.

aggregation among the catalyst in a certain reaction volume, resulting the limitation of active sites actually contacted with sulfur-containing compound.<sup>60</sup> Thus, 0.1 g catalyst was chosen as the optimal amount for ODS reaction.

To study the effect of different sulfur-containing compounds in ODS reaction over 20 wt%  $\text{WO}_x/\text{meso-SnO}_2$  catalyst. Beside DBT, benzothiophene (BT), and 4,6-dimethyl-dibenzothiophene (4,6-DMDBT), are also inflexible to be removed from fuels. The results in Fig. 7(a) indicated that the catalytic activity of these sulfur-containing compounds decreased in the order of DBT (100%) > 4,6-DMDBT (99.2%) > BT (94.4%) under the same experimental conditions. It may be ascribed to the different electron density of sulfur atoms on BT (5.739), DBT (5.758), and 4,6-DMDBT (5.760). In general, lower electron density on sulfur atom resulted in lower activity of the sulfur removal rate. Therefore, the lower electron density of sulfur atom on BT directly resulted in lowest surfur removal efficiency.<sup>61,62</sup> Moreover, compared to DBT, 4,6-DMDBT with two methyl groups on the benzene caused steric hindrance effect, leading to the active species hard to approach the sulfur atom. Therefore, the desulfurization efficiency of 4,6-DMDBT was lower than that of DBT.

To understand ODS kinetics, the kinetics parameters of DBT oxidation at different temperatures (20 °C, 30 °C, 40 °C, and 50 °C) were studied. The rate constants for the apparent consumption of DBT were obtained from the pseudo-first-order equation:

$$\ln(C_0/C_t) = kt \quad (1)$$

wherein,  $C_0$  and  $C_t$  were the sulfur concentrations at time zero and time  $t$  (min), respectively,  $k$  was the rate constant ( $\text{min}^{-1}$ ). As shown in Fig. S3(A),<sup>†</sup> a plot of  $\ln(C_0/C_t)$  versus reaction time ( $t$ ) displayed a linear relationship that confirmed the pseudo-first order reaction kinetics. The apparent rate constants of DBT were 0.0008, 0.016, 0.036 and 0.063  $\text{min}^{-1}$  at 20 °C, 30 °C, 40 °C, and 50 °C, respectively. Based on the reaction rates at different temperatures, the apparent activation energy of DBT oxidation was derived from the Arrhenius equation:

$$E_a = RT^2(\text{dln } k/\text{dT}) \quad (2)$$

$$t_{1/2} = 0.693/k \quad (3)$$

**Table 2** Rate constant  $k$ , half-live  $t_{1/2}$ , and correlation coefficient  $R$  of BT, DBT, and 4,6-DMDBT

Sulfur compound	Rate constant $k$ (min $^{-1}$ )	Half-live $t_{1/2}$ (min)	Correlation coefficient $R$
DBT	0.0631	10	0.9929
4,6-DMDBT	0.0458	15	0.9903
BT	0.0260	26	0.9951

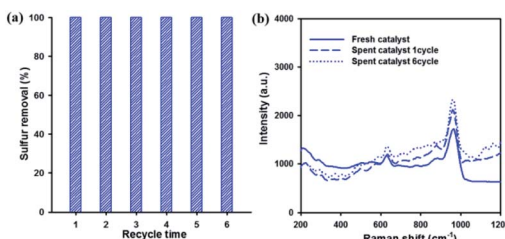


**Fig. 8** (a) Recycle tests of 20 wt%  $\text{WO}_x/\text{meso-SnO}_2$  catalyst. Reaction conditions: model oil = 14 mL, acetonitrile = 14 mL, sulfur concentration = 2000 ppm,  $n[\text{H}_2\text{O}_2] : n[\text{S}] = 5 : 1$ , catalyst = 0.1 g, reaction temperature = 50 °C, time = 60 min. (b) Raman spectra of fresh and spent catalysts.

where,  $E_a$  is the apparent activation energy,  $R$  and  $T$  are the gas constant and reaction temperature, respectively. Through the Arrhenius plot as shown in Fig. S3(B),<sup>†</sup> the activation energy of DBT is 54.8 kJ mol $^{-1}$ . Zhu *et al.*<sup>18</sup> have reported that the activation energy of DBT is 76.2 kJ mol $^{-1}$  in the polyoxometalates/H $_2$ O $_2$  catalytic system. In AcOH/H $_2$ SO $_4$ /H $_2$ O $_2$  system the activation energy of DBT oxidation is 57 kJ mol $^{-1}$ , reported by Ukkirapandian *et al.*<sup>63</sup> The oxidation kinetics of BT and 4,6-DMDBT were also investigated under the optimal conditions. The plot of  $\ln(C_0/C_t)$  versus time is shown in Fig. 7(b). Half-life was calculated by eqn (3). The rate constants  $k$  of DBT, BT, and 4,6-DMDBT were 0.0631 min $^{-1}$ , 0.0260 min $^{-1}$ , and 0.0458 min $^{-1}$ , respectively. The half-life  $t_{1/2}$  and correlation coefficients  $R$  are summarized in Table 2.

Reusability and stability of the catalyst are very important factors in industrial applications. Therefore, the reusability of the catalyst for DBT removal was investigated over 20 wt%  $\text{WO}_x/\text{meso-SnO}_2$  catalyst. After each run, the used catalyst without any treatment (*i.e.*, solvent washing, recalcination) was separated from the reaction mixture by centrifugation. Then, fresh H $_2$ O $_2$  and model oil were directly added into the original reaction round-bottom flask for the next run. Fig. 8(a) showed that the sulfur removal efficiency remained at 100% after recycling for 6 times. That is because the active tungsten species are present on the surface of meso-SnO $_2$  after recycling ODS reactions, as shown in the Fig. 8(b) Raman spectra. The results indicated that the 20 wt%  $\text{WO}_x/\text{meso-SnO}_2$  has an excellent recycling performance in the deep oxidation desulfurization.

## 4. Conclusions

Highly ordered mesoporous  $\text{WO}_x/\text{meso-SnO}_2$  catalysts with high surface area and well-defined mesoporosity were

successfully prepared by the nano-replication method and applied to oxidative desulfurization reaction for the first time. In this ODS system, through the optimization of reaction conditions, sulfur removal of DBT could reach 100% under 50 °C with 20 wt%  $\text{WO}_x/\text{meso-SnO}_2$  as catalyst. Furthermore, 20 wt%  $\text{WO}_x/\text{meso-SnO}_2$  catalysts also exhibited excellent recycling performance after recycling six times without losing catalytic activity, when the catalyst was used without any regeneration process during the recycle tests. This high catalytic activity and reusability may be ascribed to the well dispersed  $\text{WO}_x$  species and a strong interaction (synergistic effect) between  $\text{WO}_x$  and meso-SnO $_2$ . This system with a simple  $\text{WO}_x/\text{meso-SnO}_2$  catalyst has a remarkable advantage over the desulfurization by more solvent extraction and provides a promising approach for the sulfur removal in the chemical industry.

## Conflicts of interest

There are no conflicts to declare.

## Acknowledgements

This work was supported by the Education Department of Jilin Province Project of China (no. JJKH20180894KJ) and the Higher Education Discipline Innovation Project (111 Project, D18012). J. M. Kim also thanks to the Materials/Components Technology Development Program supported by the Ministry of Trade, Industry & Energy of Korea (No. 20010790).

## Notes and references

- Y. Shen, T. Sun and J. Jia, *RSC Adv.*, 2012, **2**, 3123–3132.
- P. Y. Wang, L. C. Jiang, X. Q. Zou, H. Q. Tan, P. P. Zhang, J. L. Li, B. S. Liu and G. S. Zhu, *ACS Appl. Mater. Interfaces*, 2020, **12**(3), 25910–25919.
- L. Hao, G. Xiong, L. Liu, H. Long, F. Jin and X. Wang, *Chin. J. Catal.*, 2016, **37**, 412–419.
- R. Abro, A. A. Abdeltawab, S. S. Al-Deyab, G. Yu, A. B. Qazi, S. Gao and X. Chen, *RSC Adv.*, 2014, **4**, 35302–35317.
- G. S. He, L. B. Sun, X. L. Song, X. Q. Liu, Y. Yin and Y. C. Wang, *Energy Fuels*, 2011, **25**, 3506–3513.
- W. H. Tian, L. B. Sun, X. L. Song, X. Q. Liu, Y. Yin and G. S. He, *Langmuir*, 2010, **26**, 17398–17404.
- J. Ge, Y. Zhou, Y. Yang and M. Xue, *Ind. Eng. Chem. Res.*, 2011, **50**, 13686–13692.
- D. Xu, W. Zhu, H. Li, J. Zhang, F. Zou, H. Shi and Y. Yan, *Energy Fuels*, 2009, **23**, 5929–5933.
- W. Li, H. Tang, Q. Liu, J. Xing, Q. Li, D. Wang, M. Yang, X. Li and H. Liu, *Biochem. Eng. J.*, 2009, **44**, 297–301.
- S. Maghsoudi, M. Vossoughi, A. Kheirolomoom, E. Tanaka and S. Katoh, *Biochem. Eng. J.*, 2001, **8**, 151–156.
- Z. Hasan, J. Jeon and S. H. Jhung, *J. Hazard. Mater.*, 2012, **205**, 216–221.
- G. Gao, S. Cheng, Y. An, X. Si, X. Fu, Y. Liu, H. Zhang, P. Wu and M. Y. He, *ChemCatChem*, 2010, **2**, 459–466.



13 H. Li, X. Jing, Y. Shi and L. Yu, *React. Chem. Eng.*, 2021, **6**, 119–124.

14 D. Zhao, R. Liu, J. Wang and B. Liu, *Energy Fuels*, 2008, **22**, 1100–1103.

15 X. Deng, R. Qian, H. Zhou and L. Yu, *Chin. Chem. Lett.*, 2021, **32**(3), 1029–1032.

16 Y. Chi, C. Li, Q. Jiao, Q. Liu, P. Yan, X. Liu and W.-B. Urs, *Green Chem.*, 2011, **13**, 1224–1229.

17 W. Zhang, H. Zhang, J. Xiao, Z. Zhao, M. Yu and Z. Li, *Green Chem.*, 2014, **16**, 211–220.

18 Y. Zheng, A. Wu, Y. Ke, H. Cao and L. Yu, *Chin. Chem. Lett.*, 2019, **30**(5), 937–941.

19 F. Lin, Z. Wang, J. Shao, D. Yuan, Y. He, Y. Zhu and K. Gen, *Chin. J. Catal.*, 2017, **28**, 1270–1280.

20 D. Wang, E. W. Qian, H. Amano, K. Okata, A. Ishihara and T. Kabe, *Appl. Catal., A*, 2003, **253**, 91–99.

21 W. Zhu, P. Wu, Y. Chao, H. Li, F. Zou, S. Xun, F. Zhu and Z. Zhao, *Ind. Eng. Chem. Res.*, 2013, **52**, 17399–17406.

22 C. Chen, Y. Cao, X. Wu, Y. Cai, J. Liu, L. Xu, K. Ding and L. Yu, *Chin. Chem. Lett.*, 2020, **31**(5), 1078–1082.

23 M. Te, C. Fairbridge and Z. Ring, *Appl. Catal., A*, 2001, **219**, 267–280.

24 C. Wang, Y. Qiu, H. Y. Wu, W. S. Yang, Q. Zhu, Z. G. Chen, S. H. Xun, W. S. Zhu and H. M. Li, *Fuel*, 2020, **270**, 117498–117505.

25 Y. Du, L. N. Zhou, Z. H. Liu, Z. R. Guo, X. Z. Wang and J. H. Lei, *Chem. Eng. J.*, 2020, **387**, 124056–124065.

26 C.-C. Luis, G.-B. Hilda, F.-C. Adriana, G.-G. Hector D and C.-G. Rogelio, *Catal. Today*, 2008, **133–135**, 244–254.

27 J. Zou, Y. Lin, S. Wu, Y. Zhong and C. Yang, *Adv. Funct. Mater.*, 2021, **31**, 2100442–2100453.

28 V. V. D. N. Prasad, K.-E. Jeong, H.-J. Chae, C.-U. Kim and S.-Y. Jeong, *Catal. Commun.*, 2008, **9**, 1966–1969.

29 L. F. Ramírez-Verduzco, J. A. De los Reyes and E. Torres-García, *Ind. Eng. Chem. Res.*, 2008, **47**, 5353–5361.

30 M. Zhang, W. Zhu, H. Li, S. Xun, W. Ding, J. Liu, Z. Zhao and Q. Wang, *Chem. Eng. J.*, 2014, **243**, 386–393.

31 X. Li, S. Huang, Q. Xu and Y. Yang, *Transition Met. Chem.*, 2009, **34**, 943–947.

32 M. A. Cortes-Jácome, M. Morales, C. Angeles Chavez, L. F. Ramírez-Verduzco, E. López-Salinas and J. A. Toledo-Antonio, *Chem. Mater.*, 2007, **19**, 6605–6614.

33 G. Rodriguez-Gattorno, A. Galano and E. Torres-García, *Appl. Catal., B*, 2009, **92**, 1–8.

34 J. Zou, Y. Lin, S. Wu, M. Wu and C. Yang, *Sep. Purif. Technol.*, 2021, **264**, 118434–118445.

35 W. A. W. A. Bakar, R. Ali, A. A. A. Kadir and W. N. A. W. Mokhtar, *Fuel Process. Technol.*, 2012, **101**, 78–84.

36 K. Kamata, K. Yonehara, Y. Sumida, K. Hirata, S. Nojima and N. Mizuno, *Angew. Chem., Int. Ed.*, 2011, **50**, 12062–12066.

37 Z. Zhang, Q. Zhu, J. Ding, X. Liu and W. L. Dai, *Appl. Catal., A*, 2014, **482**, 171–178.

38 Z. Ma, W. Hua, Y. Tang and Z. Gao, *J. Mol. Catal. A: Chem.*, 2000, **159**, 335–345.

39 M. Jin, J.-N. Park, J. Shon, Z. Li, M. Yoon, H. Na, Y.-K. Park and J. Kim, *Res. Chem. Intermed.*, 2011, **37**, 1181–1192.

40 T.-W. Kim, F. Kleitz, B. Paul and R. Ryoo, *J. Am. Chem. Soc.*, 2005, **127**, 7601–7610.

41 J. K. Shon, H. Kim, S. S. Kong, S. H. Hwang, T. H. Han, J. M. Kim, C. Pak, S. Doo and H. Chang, *J. Mater. Chem.*, 2009, **19**, 6727–6732.

42 J. K. Shon, S. S. Kong, Y. S. Kim, J.-H. Lee, W. K. Park, S. C. Park and J. M. Kim, *Microporous Mesoporous Mater.*, 2009, **120**, 441–446.

43 F. S. H. Simanjuntak, V. T. Widyaya, C. S. Kim, B. S. Ahn, Y. J. Kim and H. Lee, *Chem. Eng. Sci.*, 2013, **94**, 265–270.

44 B. Mallesham, P. Sudarsanam, G. Raju and B. M. Reddy, *Green Chem.*, 2013, **15**, 478–489.

45 J. H. Pan and W. I. Lee, *Chem. Mater.*, 2006, **18**, 847–853.

46 J. X. Zhou, M. S. Zhang, J. M. Hong and Z. Yin, *Solid State Commun.*, 2006, **138**, 242–246.

47 Z. Zhang, Q. Zhu, J. Ding, X. Liu and W.-L. Dai, *Appl. Catal., A*, 2014, **482**, 171–178.

48 V. M. Benítez and N. S. Fígoli, *Catal. Commun.*, 2002, **3**, 487–492.

49 Z. Ma, D. Weng, X. Wu and Z. Si, *J. Environ. Sci.*, 2012, **24**, 1305–1316.

50 Z. Hasan, J. Jeon and S. H. Jhung, *J. Hazard. Mater.*, 2012, **205–206**, 216–221.

51 M. Martos, J. Morales and L. Sanchez, *J. Mater. Chem.*, 2002, **12**, 2979–2984.

52 K. M. Parida, S. Mallick and G. C. Pradhan, *J. Mol. Catal. A: Chem.*, 2009, **297**, 93–100.

53 D. C. Vermaire and P. C. van Berge, *J. Catal.*, 1989, **116**, 309–317.

54 I. E. Wachs, C. C. Chersich and J. H. Iiardenbergh, *Appl. Catal.*, 1985, **13**, 335–346.

55 V. Benítez, C. Querini and N. Fígoli, *Appl. Catal., A*, 2003, **252**, 427–436.

56 J. Horsley, I. Wachs, J. Brown, G. Via and F. Hardcastle, *J. Phys. Chem.*, 1987, **91**, 4014–4020.

57 Z. Li, H. J. Jeong, K. Sivarajanji, B. J. Song, S. B. Park, D. Li, C. W. Lee, M. Jin and J. M. Kim, *Nano*, 2015, **10**, 1550075.

58 J. Zhang, A. Wang, X. Li and X. Ma, *J. Catal.*, 2011, **279**, 269–275.

59 S. S. Wang and G. Y. Yang, *Chem. Rev.*, 2015, **115**, 4893–4962.

60 H. Li, L. He, J. Lu, W. Zhu, X. Jiang, Y. Wang and Y. Yan, *Energy Fuels*, 2009, **23**, 1354–1357.

61 W. Ma, Y. Xu, K. Ma and H. Zhang, *Appl. Catal., A*, 2016, **526**, 147–154.

62 H. Lü, J. Gao, Z. Jiang, F. Jing, Y. Yang, G. Wang and C. Li, *J. Catal.*, 2006, **239**, 369–375.

63 Y. Shiraishi, K. Tachibana, T. Hirai and I. Komasawa, *Ind. Eng. Chem. Res.*, 2002, **41**, 4362–4375.

